

IMPERIAL COLLEGE LONDON

Solar Wind Proton Measurements with Parker Solar Probe

A. Giroul

supervisor
Prof. T. S. HORBURY

A thesis submitted in fulfilment of the requirements for the degree of Master of Science
in Physics and the Diploma of Imperial College London

10th September 2018



Artist's rendering of Parker Solar Probe leaving Earth.
Credit: Johns Hopkins University Applied Physics Laboratory.

Abstract

Parker Solar Probe will take measurements of particles in the solar wind plasma with the SWEAP instrument suite ([1]). The spacecraft's solar shield restricts the field of view on the plasma. This report presents a detailed description of the SWEAP proton instruments and their limitations. A model of the instrument outputs is presented, showing how to simulate measurements. It is shown that a 700km s^{-1} solar wind will be in the frame of view of the SPAN-A instrument for 13 days during the mission; simulations at 35 and 13 solar radii show that alfvénic fluctuations can shift the solar wind into the field of view.

Contents

Introduction	5
1 Exploring the Inner Heliosphere	6
1.1 The Sun and the Solar Wind	6
1.2 The Parker Solar Probe Mission	7
1.3 The Solar Wind Protons	8
2 Plasma Instruments	9
2.1 Solar Probe ANalysers (SPAN)	10
2.1.1 Basis of Functioning	10
2.1.2 SPAN-A Specifications	11
2.1.3 SPAN-A Orientation and Field of View	11
2.2 Solar Probe Cup	12
2.2.1 Faraday Cups	12
2.2.2 Solar Probe Cup Specifications	13
2.2.3 Angular Response from SPC	13
3 Simulating Measurements	17
3.1 Modelling the Solar Wind	17
3.2 Modelling SPAN-A Measurements	18
3.3 Modelling SPC Measurements	19
3.4 Realistic Solar Wind Conditions	19
4 Results & Analysis	20
4.1 Mission Statistics	20
4.2 Scenario Analysis	22
4.3 Discussion	25
Conclusion	26
References	26
A Appendix	28
A.1 Maths & Derivations	28
A.1.1 Notation	28
A.1.2 Area of a Disc Section	28
A.1.3 Rodrigues' Rotation Formula	28
A.2 Acknowledgements	29
A.3 Declaration of Work	29

Introduction

At the time of writing, Parker Solar Probe is 28 million kilometres away from Earth, travelling at more than 75 000 kph on route towards our star, the Sun. Parker Solar Probe (PSP)¹ was launched on 12th August 2018; it will be the first spacecraft to touch the Solar corona. Approaching a star comes with an obvious challenge: PSP needs to be protected from solar radiation. The 50 year delay between the concept and execution of this mission is evidence that this is not an easy obstacle to overcome. [2, 3]

PSP will take measurements of the *solar wind*: a tenuous, hot, magnetised plasma streaming continuously from the Sun. It fills the interplanetary space of the solar system, delimiting a zone known as the *heliosphere*, which extends beyond all the planets. While its existence was hinted at much earlier², a convincing model was presented by Eugene Parker in 1958. It remained controversial until actual measurements of the wind were taken.

As well as giving a more complete profile of how the solar wind (SW) changes as it flows outwards, PSP plasma measurements will reveal signatures of waves and turbulence, as well as their correlation to phenomena observed on the Sun's surface. Proximity to the Sun is key for these observations, as some features get smoothed out in the plasma stream.

PSP will take pictures of the solar corona, measure the electromagnetic fields and plasma particles. This project focusses exclusively on the latter: the *SWEAP* plasma instruments suite which is presented in Kasper et al. (2015) (hereafter K15) [1]. SWEAP stands for *Solar Wind Electrons and Protons*, but in fact measures all charged particles. This project, however, restricts its focus to protons.

SWEAP has two instruments that measure SW protons: SPAN-A (*Solar Probe ANalyser*. 'A' refers to the proton version of the instrument) and SPC (*Solar Probe Cup*). The former has a restricted field of view due to its placement behind the spacecraft's heat shield. This is necessary for the instrument not to overheat through solar radiation. The latter, while facing the Sun directly, provides very little directional information about the protons. [1]

The aim of this project is to present and model both instruments, to compare them and highlight challenges related to limited fields of view. Additionally, it is shown how the solar wind can shift in and out of the SPAN-A field of view over the course of the PSP mission - due to both a changing velocity of the spacecraft, and alfvén fluctuations in the solar wind. Both these can help observe the plasma properties by shifting the SW direction into the field of view.

¹PSP was previously referred to as Solar Probe Plus (SPP) before being renamed in honour of the astrophysicist Eugene Parker.

²Cassini hypothesised a dust cloud around the Sun in 1672; scientists such as Bessel, Carrington, and later Birkeland, Lindemann and others worked on understanding the aurora and geomagnetic activity. For a history of solar wind science, see Brandt (1970) [4].

In the next section (1), some of the physics that PSP is expected to observe will be introduced, as well as the science objectives of the mission and how these relate to measuring plasma properties. Some relevant aspects of this space mission will also be discussed. Then, section 2 will provide a description SPAN-A and SPC as well as their fields of view. Section 3 shows how to simulate proton measurements, by modelling both the instruments and a simplified solar wind. Finally, section 4 will present simulation results and an analysis of how well the SW can be observed throughout PSP's 7-year trajectory.

A picture of Parker Solar Probe can be seen on page 3, featuring its heat shield, SPAN-A and SPC.

1 Exploring the Inner Heliosphere

1.1 The Sun and the Solar Wind

The interplanetary medium is dominated by the solar wind plasma flow. This magnetised flow has structure on all scales: from the large spiral shaped by the magnetic field due to the Sun's rotation, to plasma waves and turbulence at kinetic levels. The SW is essentially an extension of the Sun's outer atmosphere, the *corona*, which cannot be in hydrostatic equilibrium. The corona is much hotter and tenuous than the visible solar surface - the *photosphere*. It is too faint to be observed from Earth, except during solar eclipses. The wind starts as a subsonic flow in the corona and out to a critical radius after which it remains supersonic³ to the edge of the heliosphere, where its ram pressure⁴ is finally balanced by the interstellar medium. [5]

The solar wind, while primarily constituted of electron and protons, also contains some other ions, primarily α particles (helium nuclei). Their concentration varies but is usually around 4% [6]. For simplicity only protons are considered in this report. The flow speed of the wind varies; it is usually categorised into two types. The slow wind, more variable, has speeds between 250-400km s⁻¹, while the fast wind flows at 750km s⁻¹ [7]. There are also transient flows, such as coronal mass ejections, which can have much larger velocities. During solar maximum both types of wind arise at all solar latitudes. In contrast, during solar minimum (such as during most of the PSP mission) the Sun's polar regions show almost exclusively steady fast wind, while the equatorial regions feature only a few zones of fast wind, above region of open magnetic field lines⁵, *coronal holes*. [5, 8]

Energy from the Sun's interior is transferred to the surface through convection, but how is this energy transferred to the much less dense corona and wind? An energy transfer clearly occurs, evidenced by the very high temperatures in the corona and high wind speeds. The plasma is non-collisional⁶ - energy is transferred through electromagnetic interactions such as waves and instabilities. Evidence of these kinetic processes can be seen in the particle populations, more specifically, their velocity distribution. Dissipative processes in the plasma, which becomes non-ideal past about 20 solar radii, can erase those structures as energy is transported to smaller scales. The time structure of events is also disturbed, as particles travel at different speeds in the wind and end up flowing alongside other particles not emitted in the same process. This is why a mission to observe the SW as close to the Sun as possible is scientifically crucial. [2]

³Supersonic (subsonic) means that the plasma's bulk velocity is larger (smaller) than the plasma particles' mean thermal speeds.

⁴Pressure originating from its bulk momentum.

⁵Most of the magnetic fields lines in the corona are closed, forming loops.

⁶Meaning collisions affect the plasma only on relatively larger time-scales, other interactions have larger effects on relevant time-scales. [6]

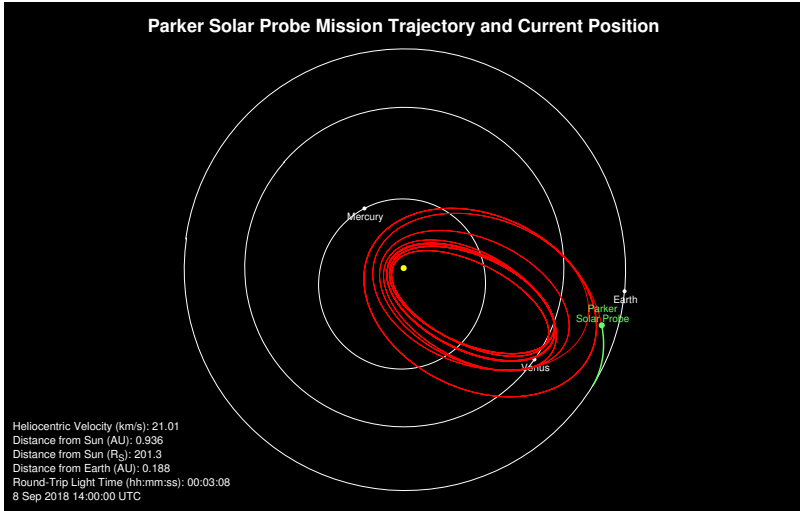


Figure 1: Parker Solar Probe planned trajectory, along side the inner planets' orbits. The green part of the trajectory is already completed at the time of writing, 27 days after launch. Credit: Johns Hopkins University Applied Physics Laboratory. [3]

1.2 The Parker Solar Probe Mission

Parker Solar Probe will take measurements from 54 down to 10 solar radii while orbiting the Sun in a highly elliptical orbit. The planned trajectory of the probe over its mission is shown in figure 1. The most crucial parts of the orbit are near perihelion; the first of these will happen 3 months after launch, in early November 2018 [3]. Note that each successive orbit gets somewhat closer to the star at perihelion. The spacecraft uses the planet Venus to gravity assist it into closer orbits. In each orbit, measurement setting for the next approach are configured before entering the 'primary science' zone below 54 solar radii, as communication links with the spacecraft are limited near perihelion. [2]

PSP is protected from the sun by a 'thermal protection system', a carbon shield that stops the solar radiation from damaging it. This heat shield is visible behind the spacecraft in the picture on page three, as well as at the top of the schematic spacecraft in figure 2. PSP has to remain in a stable trajectory with the shield facing the Sun; this is achieved using reaction wheels storing unwanted angular momentum. The position of the sun is kept track of by sensors and the wheels activated accordingly. [2]

The schematic representation of the spacecraft in figure 2 shows approximate positions of the two SWEAP proton instruments: SPC, in blue, at the edge of the thermal shield, and SPAN-A, in red, on the main body of the probe. In this diagram, the sun is towards the top of the page; the spacecraft is travelling to the right. The yellow lines represent the solar wind stream, not the sun's (photon) radiation. Both are travelling radially in the sun frame; however, in the moving *spacecraft frame*, the solar wind acquires a 'headwind' velocity, hitting the spacecraft sideways. Photons, travelling about a thousand times faster, always hit the spacecraft head on. This is important, as it allows SPAN-A to sample the solar wind plasma while protected from the damaging solar radiation (as seen in figure 2) However, this is only possible when the spacecraft travels sufficient azimuthal speed, or if, as will be seen in the section below, the solar wind velocity itself acquires a azimuthal component form its fluctuations.

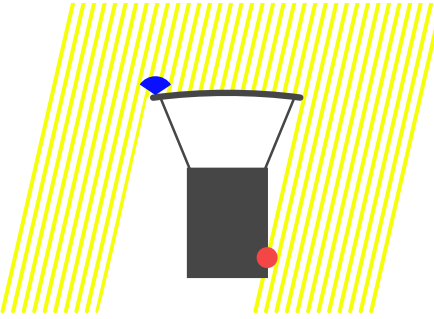


Figure 2: Schematic view of instrument positions. The solar wind in the spacecraft frame is shown in yellow; SPAN-A is in red and SPC in blue. The former will only sample the wind coming in at an angle from the radial sun direction (top of this figure).

1.3 The Solar Wind Protons

Properties of a particle population can be quantified in terms of a *velocity distribution function* (VDF). Generally, this is a function defined for a given particle species (here protons), that gives the differential density of particles at a given velocity. This can vary in time and space, and so the VDF can be written as

$$f = f(\vec{v}, \vec{r}, t) , \quad (1.1)$$

a function of time t , position \vec{r} and velocity \vec{v} . Usually the dependence on t and \vec{r} is implied and the VDF is written as $f(\vec{v})$. Integrating $f(\vec{v})$ over a volume of velocity space gives the number density of particles in that velocity range. Thus, the VDF is in units of $\text{m}^{-3}(\text{m/s})^{-3}$ or m^{-6}s^3 . It follows that its zeroth moment is equal to the total particle number density n , i.e.

$$n = \int f(\vec{v}) d^3 v , \quad (1.2)$$

where the dependence on time and position is also implied. The integration is performed over all velocity space. Higher moments define the density and energy fluxes, pressure, and temperature tensors. [9]

The velocity distribution of solar wind protons is anisotropic. This is possible due to the long time scales of collisions in the tenuous wind[6]. It can be reasonably modelled by a core bi-Maxwellian distribution (see equation 3.1) and a high velocity beam along the magnetic field direction. Only about 10% of the proton density is found in the beam for slow solar wind, and 4% for the fast wind. The temperature of the core distribution is lower parallel to the magnetic field - particles have higher thermal velocities orthogonally to the field direction. See figure 3 for a cut through a (three dimensional) proton VDF. [10]

While the magnetic field in the solar wind has, on heliospheric scale, a direction forming an Archimedean spiral [5] (the so-called *Parker spiral*), corresponding to a 45° angle from the radial direction [10], on smaller scales the field can be in any direction due to plasma waves. Waves and turbulence in the wind can not only rotate the magnetic field direction, but also the mean bulk velocity of the wind. This is relevant for this work; as described above, the incoming SW direction will determine whether it can be sampled by the instruments. It has been known for a long time (Belcher and Davis (1971) [11]) that fluctuations in bulk velocity and magnetic field are often correlated, especially in fast wind streams. This observed correlation can be expressed as

$$\delta\vec{v} \simeq \pm \frac{\delta\vec{B}}{\sqrt{4\pi\rho}} , \quad (1.3)$$

where \vec{v} is the change in solar wind velocity, \vec{B} in magnetic field and $\rho = m_p n$ is the mass density of the plasma. It has been confirmed to exist ubiquitously and over a wide range of time-scales. [12]

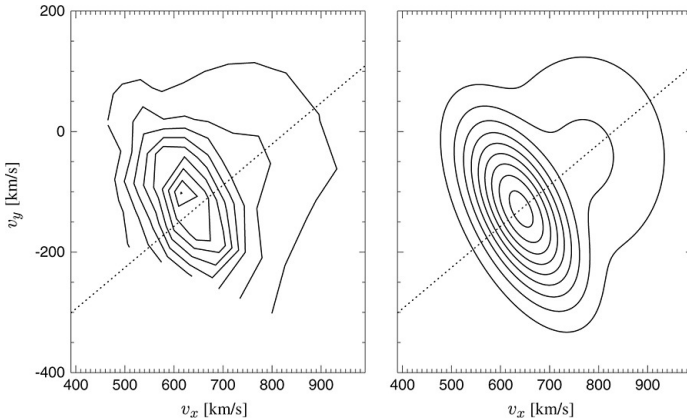


Figure 3: Slice through a proton VDF as observed by Helios 2 at 0.3 AU (left), and fit of this VDF by a bi-Maxwellian and beam model (right). The magnetic field direction is shown as a dotted line. Notice how the core distribution is ‘squashed’ along the magnetic field direction – the temperature is smaller along it. Figure taken from Hellinger et al. (2013) [10].

These fluctuations are Alfvénic.; equation 1.3 can be rewritten as [7]

$$\frac{\delta \vec{B}}{|B_0|} = \pm \frac{\delta \vec{v}}{V_A} \quad , \quad (1.4)$$

where B_0 is the initial magnetic field, and the *Alfvén speed*, V_A , is

$$V_A = \frac{|B_0|}{\sqrt{4\pi\rho}} = \frac{|B_0|}{\sqrt{4\pi n m_p}} \quad . \quad (1.5)$$

Alfvén waves are transverse: they disturb the magnetic field and plasma perpendicularly to their direction of propagation [5]. They act on the magnetic field similarly to waves on a string, keeping its magnitude constant but changing its direction. This means that

$$|\delta \vec{B} + \vec{B}_0| = |B_0| \quad ; \quad (1.6)$$

the magnetic field moves on a circle. Occasionally it can rotate by a full 180° in what is referred to as a *switchback*; in that case the ratio $|\delta B||/|B_0|$ reaches its maximum magnitude of 2. [7]

Consequently, according to 1.4 the change in SW velocity can have magnitude

$$|\delta \vec{v}| \leq 2V_A \quad (1.7)$$

with a direction defined by the magnetic field direction change.

2 Plasma Instruments

In this section the SPC and SPAN-A will be described so that the simulation model in section 3 can be developed. The differences between both instruments will also be highlighted.

2.1 Solar Probe ANalysers (SPAN)

2.1.1 Basis of Functioning

SPAN-A is a so-called *top-hat* electrostatic analyser (ESA).⁷ This type of instrument was developed by Carlson et al.(1982)⁸. It is a very powerful instrument, having an almost 4π directional coverage, and distinguishing incoming particles' directions (both in term of azimuthal and elevation angles) and energies - essentially resolving a three dimensional velocity distribution function. [13]

The instrument consist of two semi-spherical metallic plates separated by a thin gap, with a (covered) opening at the top (hence *top-hat*). An electric field is applied between the plates. Energy selection is made by varying this field: particles with the correct energy per charge ratio are deflected such that their radius of curvature matches the plates; they continue their route and hit the detectors. This is shown in figure 4. The detectors are arranged in a ring below the semi-sphere, and hence provide the azimuthal incoming direction ϕ of a particle. [9] The detectors are *microchannel plates* (MCPs) - a set of tiny tubes with a large voltage applied. When an ion hits the surface, it causes electrons to be emitted in one of the tubes - these will inevitably (by design) hit another surface, causing more electron emission and resulting in an avalanche of electrons. In such fashion the signal from a single particle (a *count*) can be recorded electronically. [12]

At the entrance of the top-hat, particles from a chosen acceptance angle θ range are collimated to the right orientation to enter the detector - other particles are effectively prevented from this. [9] The acceptance angle can be modified by applying an additional electric field to deflect incoming particles. In the following section, a few technical details for SPAN-A from K15 will be summarised.

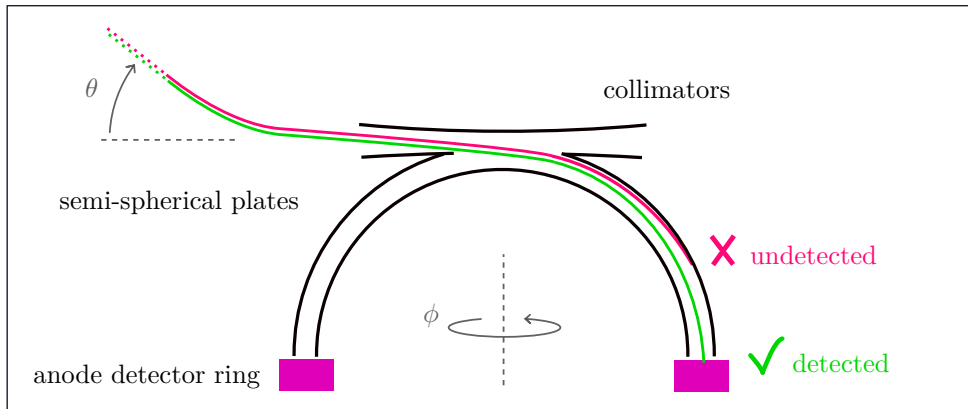


Figure 4: A schematic diagram of an electrostatic analyser. Shown is a cross-section through the centre of the semi-spherical instrument. Two proton paths are drawn, one in the energy band being measured (in green) and one with a greater energy (in red), which is not detected in this setting. Both protons come from the same direction, but the acceptance range of θ can be modified by the electrostatic deflectors (not pictured). A more technical drawing showing the deflectors, can be found in K15 [1], fig. 24.

⁷For an alternative description & diagram of a top-hat ESA, see Bruno and Carbone (2005) [12], section 16.1.

⁸While electrostatic analysers have been used as early as the 1960s, e.g. in the Mariner 2, IMP, Vela and Pioneer space missions [4], top-hat ESAs have advantage over previous instruments - their cylindrical symmetry gives them a uniform azimuthal response. [13]

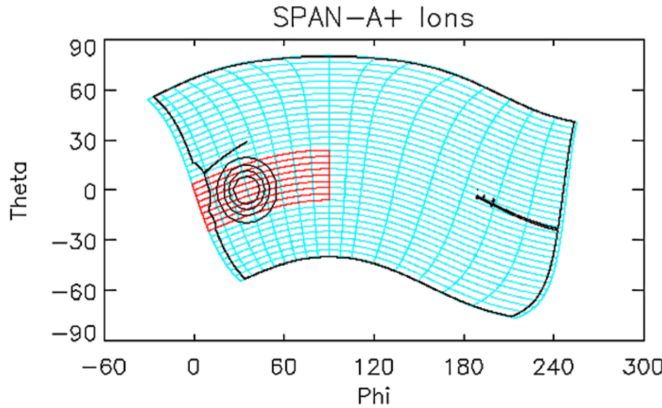


Figure 5: The field of view of SPAN-A. The 'pixels' available to the instrument are shown in blue and red, while the black border shows limits to the field of view. Notice how the first anode band (column of pixels) near $\phi = 0$ is partially obstructed. Image taken from K15 [1]

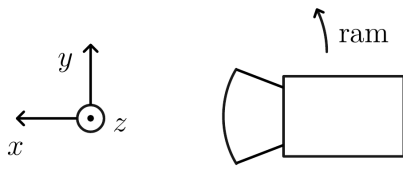


Figure 6: Local cartesian frame used, looking from above the ecliptic plane. z points out of the page, out of the ecliptic plane. It is also the direction of the angular momentum of the spacecraft's orbit. The spacecraft (pictured, with its shield towards the Sun) is travelling in the y direction, and x points towards the Sun. Note that this coordinate system is left-handed.

2.1.2 SPAN-A Specifications

SPAN-A has 16 detector anodes, adding to a 247.5° azimuthal field of view. Ten out of these detectors, corresponding to directions of incoming solar wind, are 11.25° wide, while the remaining six are 22.5° wide. It can accept particles coming from up to $\theta = \pm 60^\circ$ from the detector plane (θ as shown in figure 4). This is split in $22 \times 3.75^\circ$ deflection acceptance angles. This can be seen in figure 5, reproduced from K15 [1]. The angles are distorted because they are shown in an ecliptic frame, rather than instrument frame (this will be discussed in the following section, 2.1.3). The instrument does not operate at full resolution: it has multiple modes, e.g. scanning only the relevant part of the field of view (shown in red in figure 5), or skipping some deflection bands. It is also equipped with two attenuators which can diminish incoming flux by a factor of 10 or 100 if necessary. [1]

The instrument can detect particles from $\sim 5\text{eV}$ up to 30 KeV (per elementary charge), but note that above $\sim 4.5 - 6.0\text{ KeV}$, particles cannot be detected in the full 120° deflection range. The energy resolution is $\Delta E/E \sim 7\%$. Particle counts are read out every 0.5 ms . SPAN-A also has a time of flight section (not described here) that can determine the mass of an ion, allowing the instrument to separate signals from each ion type. In contrast, SPC does not have this capability. [1]

2.1.3 SPAN-A Orientation and Field of View

Since PSP does not rotate (as discussed in 1.2), its field of view will remain the same in a local ecliptic frame. Such a frame can be seen in figure 6. It shows x towards the Sun, y towards the ram direction (direction of travel of the azimuthal travel of the spacecraft around the Sun) and z upwards from the ecliptic plane.⁹ Note that often variations are used, e.g. with z towards the sun, so it is important to check which system is being used.

⁹Upwards as it is usually defined, such that the orbit of the Earth (and of the spacecraft) have a positive rotation vector.

To define the orientation of SPAN-A in these coordinates, one needs two perpendicular unit vectors: \vec{n} , defining the $\theta = 90^\circ$ direction, i.e. the top of the detector (as it is shown in figure 4); \vec{m} , pointing in the direction of $\phi = 0^\circ$ and $\theta = 0^\circ$ i.e. the direction where the anode detectors start, in their plane. These are found to be

$$\vec{n} = (+0.00 \quad +0.35 \quad -0.94) \quad (2.1)$$

$$\vec{m} = (-0.39 \quad -0.86 \quad -0.32) \quad (2.2)$$

in the coordinate system of figure 6. This corresponds to \vec{n} pointing at 70° down from the ram direction (y axis), in the $y-z$ plane. Looking at the image of PSP on page 3, and noting that SPC is on the anti-ram side (to $-y$), one can note the rough orientation of SPAN-A and how \vec{n} given above is realistic. These values are not available in the literature, they have been recovered by rotating coordinates until a figure identical to 5 is obtained. To compare the figures, they have simply been superimposed on a computer. The precision obtained with this simple technique should be of about 1° . Note that while the detectors start in the \vec{m} direction, they end directly towards the sun, in the x direction¹⁰ (1, 0, 0). However, the last detector has a partially obstructed view, as can be seen on figure 5 - it is about half to fully obstructed, depending on which deflection band one is looking at (the black line on the figure shows the edge of obstructions). In other words, SPAN-A only has a view of the plasma coming at an angle larger than $\sim 5.5^\circ - 11.25^\circ$ of the line of sight to the Sun.

2.2 Solar Probe Cup

2.2.1 Faraday Cups

Faraday cups (FCs) essentially work by rejecting particles below a chosen energy threshold, applying an electric field that prevent these from hitting the detector. A diagram of a Faraday cup is shown in figure 7. The detector plates measure a *current* of charged particles that hit it (as opposed to the counts measured by the MCP in a electrostatic amplifier). This means a Faraday cup signal is reliable and stable over long periods of time[14], as well as being able to measure high particle fluxes¹¹. [15]

While FCs usually provide no directional information, Solar Probe Cup does to some extend - this is discussed in the section below (2.2.3). What is true for all FCs is that they only distinguish energies perpendicular to the plane of the cup - providing a reduced distribution¹². This is quite limiting, especially compared to the intrinsically three-dimensional data provided by a top-hat ESA. Lastly, note that SPC has no way of distinguishing particles with the same energy per charge ratio - data from e.g. alpha particles will have to be identified manually.

To understand the functioning of a Faraday cup, refer to figure 7. Ions enter through the top of the instrument through a first grid (1). Then, they arrive in a zone of upward electric field (in red) which will expel the particle out of the detector, if it is not fast enough. Faster particles are merely deflected, but reach the high voltage modulator grid (3), after which an equal and opposing electric field pushes them back to their original speed and direction. Lastly, the particles go through the limiting aperture, some additional grids (5), and hit the collector (detector) plates (6) in which they create an electric current. The suppressor grid (5) is kept at a low voltage to repulse lower

¹⁰This is easy to check: $\vec{m} \times \hat{x} = \vec{n}$ so they are both the same plane perpendicular to \vec{n} and $\arccos(\vec{m} \cdot \hat{x}) = \pm 113^\circ = \pm 247^\circ$ which is the coverage of the detector.

¹¹MCPs can get saturated, and counter electronics can get paralysed at high count rates. [9]

¹²VDF integrated along one, or as in this case two dimensions; resulting in a one dimensional distribution.

energy electrons which have been reflected inside the detector. The voltage of the modulator grid can be varied to detect particles of chosen energy. [1]

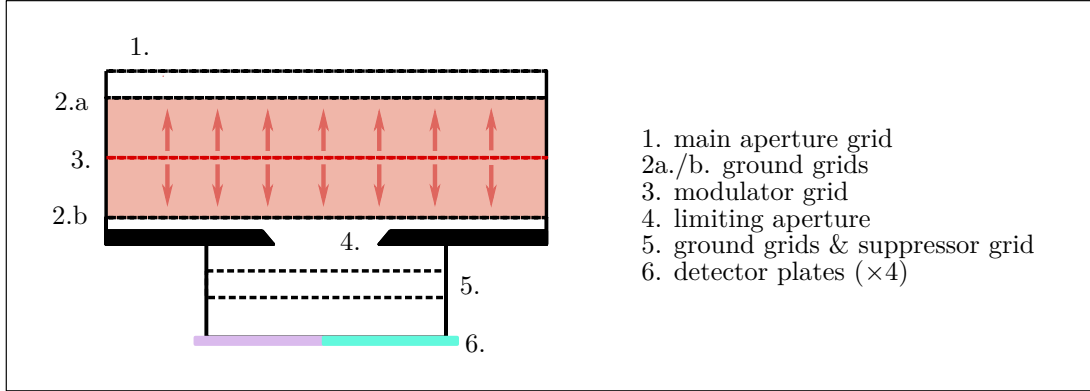


Figure 7: Schematic diagram of the Solar Probe Cup. The red arrows and shading show the direction and presence of the electric field. Figure based on fig.17 in K15 [1].

The electric field that filters out particles is created by a high voltage applied to the modulator grid; this voltage can be adjusted to accept the required particle energies. In fact, if the voltage is varied as a wave between two values this allows a measurement of particles only *between* the two corresponding energies. Indeed, in this scenario, particles with energies above this band still hit the detector; however only particles with intermediate energies will show up as modulated signal with the same signature as the input voltage. This modulated signal can be easily extracted. This gives a more direct distribution (as opposed to the integral of the distribution *up to* the chosen energy that would occur with a constant voltage). Additionally, it allows to easily subtract constant sources of false signal, such as photoelectrons and electrons from the plasma¹³. [15] Thus, effectively, a Faraday cup can scan through the reduced velocity distribution function.

2.2.2 Solar Probe Cup Specifications

The modulated voltage of SPC can be changed from -2kV to $+8\text{kV}$, with an adjustable wave amplitude between $50 - 800\text{V}$ (at 1280Hz). It can detect particles in a range of 100eV up to 8keV , with an energy resolution $\Delta E/E < 10\%$. SPC faces the sun directly and is located on the anti-ram side of the spacecraft. For completeness, note that its orientation can be written in the same way as for SPAN-A in section 2.1.3 as $\vec{n} = (+1 \ 0 \ 0)$ and $\vec{m} = (0 \ -1 \ 0)$.

2.2.3 Angular Response from SPC

SPC does provide some directional information. In fact, its circular detector plate is split into four collector 'pixels'. To understand how these correspond to incoming angles, let us consider a beam of unidirectionally travelling protons into the cup. Only protons that travel through the limiting aperture will reach the detector plates. It is also important to note that while the protons get diverted by the electric field of the cup, they go through an equal and opposite field, meaning they recover their original direction of travel. This can be seen in figure 8 (left) - notice how angle t is recovered below the limiting aperture.

¹³These enter the cup easily as they are neutral/negatively charged.

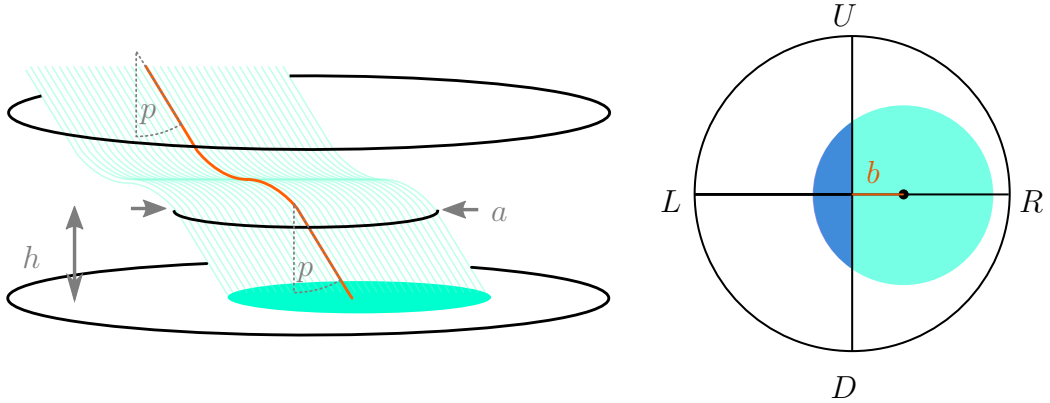


Figure 8: Geometry of the Faraday cup, showing, on the left, paths of a directional proton beam into the cup (with one highlighted path). The three rings are, starting from the top, the main aperture, the limiting aperture, and the detector plate respectively (c.f. figure 7). On the right, the surface of the detectors hit by this beam and its spread across the four plates. The four letters *U*, *R*, *D* and *L* stand for *up*, *right*, *down* and *left* respectively.

The 'illuminated' surface on the detector plates is shown on the right part of the figure. What fraction of this surface lies on each detector? Typically [16], only the following signal ratios are considered:

$$V \equiv \frac{U - D}{U + D} \quad \text{and} \quad W \equiv \frac{R - L}{R + L} \quad (2.3)$$

where *U* is the combined signal from the two *upper* plates of the instrument, *D* from the two lower (*down*) plates, *R* the two *right*, and *L* the two *left* plates.

Suppose, at first, that the proton beam is coming from the left at angle *t* from the vertical, as in figure 8 (refer to this figure in the following). Immediately, we can say that the radius of the area is the same as the radius of the limiting aperture, *a*, and that the distance between the two circles' centres is *b* = *h* tan(*t*), where *h* is the distance between the limiting aperture and the detectors. Additionally, the relative signal ratio *W* is equal to the relative ratio of the teal area to the blue area. This ratio is shown to be (see A.1.2 in the appendix) :

$$H(x) = 1 + \frac{2}{\pi} (\sin(x) \cdot \cos(x) - x) \quad (2.4)$$

where

$$a \cos(x) \equiv b \quad (2.5)$$

(in which *a* and *b* are defined as above). And so,

$$W(p) = H(\arccos[m \cdot \tan(p)]) \quad (2.6)$$

where *m* ≡ *a/h*. For SPC, *m* = 1.51 [16].

Now, consider a more general case, where the beam comes from any direction. K15 [1] note that the beam never extends further than the detector plates, and thus one can see that shifting the beam up or down (figure 8, right) would not change the ratio *W(p)*. So, for a beam having an angle

p along the $L - R$ axis, and an angle t along the $D - U$ axis, we have

$$\begin{aligned} V(t) &= H(\arccos[m \cdot \tan(t)]) \\ \text{and} \quad W(p) &= H(\arccos[m \cdot \tan(p)]) \quad . \end{aligned} \quad (2.7)$$

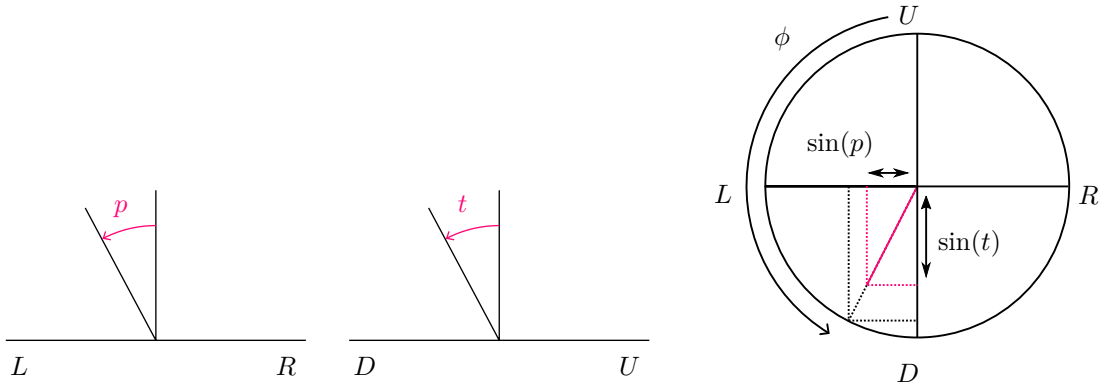


Figure 9: Geometry of the Faraday cup incoming angles. The diagram on the right shows the SPC from above, with its four pixels. The two diagrams on the left show the cup edge-on, as seen from D and R respectively, with the normal to the detectors as well as an incoming proton path. On the right hand side, we see the projection onto the plane of the detector, in red. This projection causes the $\cos(\theta)$ factors in equations 2.8.

To define angles p and t more clearly, let us express them in terms of a spherical polar coordinate system (θ, ϕ) with θ the elevation from the plane of the detectors, and ϕ azimuthal angle starting at the *up* position of the detectors. This can be seen in figure 9. From this figure, one can also see that

$$\begin{aligned} \sin(p) &= \cos(\theta) \sin(\phi) \\ \text{and} \quad \sin(t) &= -\cos(\theta) \cos(\phi) \quad , \end{aligned} \quad (2.8)$$

i.e.

$$p = \arcsin[\cos(\theta) \cdot \sin(\phi)] \quad (2.9)$$

$$\text{and} \quad t = -\arcsin[\cos(\theta) \cdot \cos(\phi)] \quad . \quad (2.10)$$

One thing to note is that equations 2.7 can be approximated by the linear functions

$$V(t) = \frac{t}{30^\circ} \quad \text{and} \quad W(p) = \frac{p}{30^\circ} \quad . \quad (2.11)$$

This is valid for small angles. SPC has an angular range of $\pm 30^\circ$ from the vertical; figure 10 shows how close this approximation is in this range.

Lastly, one needs to consider the varying effective area of the cup. Indeed, while the illuminated area of the detector does not change¹⁴ (it is a circle of diameter a), the *effective area* changes:

¹⁴Unless it is cropped by the main aperture. K15 [1] note that the illuminated area cannot extend past the collector plates, so the main aperture is the only other way it could be cropped - provided particles incoming at a large angle from normal incidence.

Figure 10: Validity of linear approximation for V and W . The blue line is $V(t)$ - or equivalently, $W(p)$ - in terms of equation 2.11 while the red line is according to the full expression 2.7.

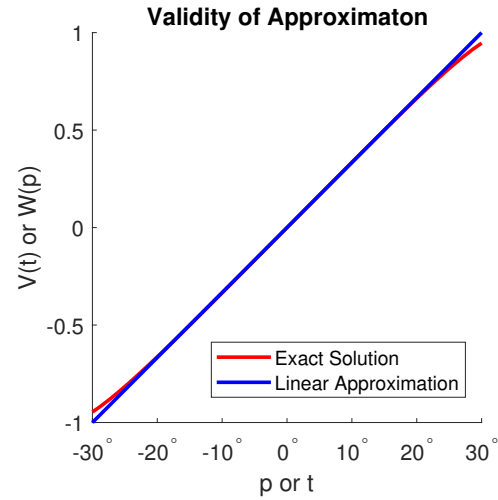
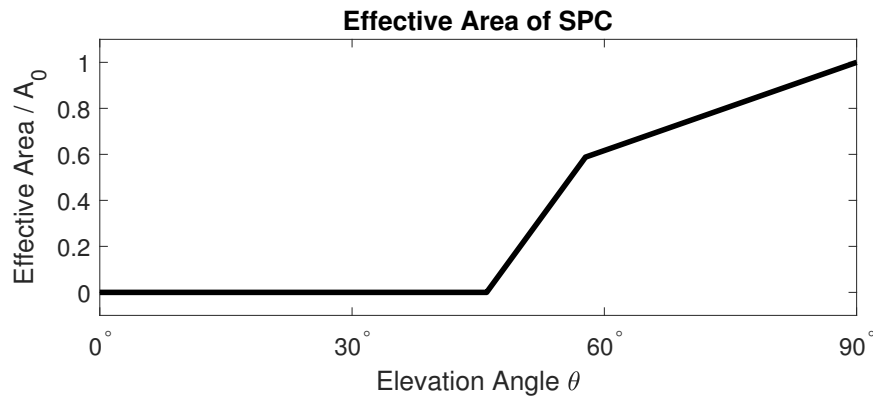


Figure 11: Effective area angular dependence for the SPC.



from a proton's perspective, the area hit is elliptical, with area depending on its incoming elevation angle. The effective area, A , is measured to follow, to about 1% [16]

$$A = A_0 \cdot \min \begin{cases} 1 - 1.15 (\theta/90^\circ) \\ 1 - 4.5 (\theta - 24^\circ)/90^\circ \end{cases} \quad (2.12)$$

which is shown in figure 11. Here, 'min' denotes the minimum between the two functions. The effective area at normal incidence, $A_0 = 136.232 \text{ mm}^2$ [16]. Notice that this extends past 60° ; the steeper slope below that might indicate a cropping of the illuminated area by the main aperture edge. While the analysis done in this work uses $A(\theta)$ as given here, the simulations described in section 3 can be performed with any elevation angle θ dependence for the effective area.

3 Simulating Measurements

A few assumptions are made in these simulations. Firstly, that the velocity distribution does not vary over the time-scale of a measurement; additionally that it does not vary in space over the distance covered by the spacecraft over this time-scale. It is also assumed that the only ions present are protons; this is of course not correct, however the simulation can easily be extended to other ions by considering their contribution independently.

3.1 Modelling the Solar Wind

The Solar Wind is modelled as a bi-Maxwellian distribution (without beam) with a bulk velocity (the wind velocity). A three-dimensional Maxwellian VDF is expressed as (see e.g. [5])

$$f(v_x, v_y, v_z) = \frac{n}{\sqrt{T_x T_y T_z}} \left(\frac{m_p}{2\pi k_B} \right)^{3/2} \exp \left(-\frac{m_p v_x^2}{2k_B T_x} - \frac{m_p v_y^2}{2k_B T_y} - \frac{m_p v_z^2}{2k_B T_z} \right), \quad (3.1)$$

where n is the number density in m^{-3} , m_p is the particles (in this case, proton) mass in kg and k_B is the Boltzmann constant (in kg/J). If one chooses z to be along the magnetic field direction, then one can write

$$T_x = T_y \equiv T_\perp \quad \text{and} \quad T_z \equiv T_\parallel, \quad (3.2)$$

the perpendicular and parallel temperatures respectively. To express $f(\vec{v})$ in the ecliptic frame, one needs to rotate the coordinates into the magnetic field direction \vec{B} . That is

$$f_e(\vec{v}) = f \left(\mathbf{R} \cdot \vec{v} - \vec{V}_{\text{SW}} \right); \quad (3.3)$$

here f is defined as in equation 3.1, and f_e is the velocity distribution function in an ecliptic frame. The matrix \mathbf{R} is the transformation that rotates \vec{B} to the ecliptic \hat{z} direction; \vec{V}_{SW} is the solar wind bulk velocity vector, in ecliptic coordinates.

The matrix \mathbf{R} can be expressed in terms of a rotation around axis $\vec{\omega}$ by an angle α , given by:

$$R_{ij} = \delta_{ij} \cos(\alpha) - \epsilon_{ijk} \omega_k \sin(\alpha) + \omega_i \omega_j (1 - \cos(\alpha)), \quad (3.4)$$

where index notation has been used; δ and ϵ having their usual meaning¹⁵. To see \mathbf{R} in matrix notation, as well as getting this expression from the Rodrigues' rotation formula, see the appendix,

¹⁵Respectively the Kronecker delta and Levi-Civita symbol.

section A.1.3. The values for $\vec{\omega}$ and α can be easily obtained from the cross and dot product of \vec{B} and \hat{z} .

The next step is to express the velocity distribution in the detector frame. This is a very similar step; the VDF needs to be shifted by the spacecraft velocity and rotated into the instruments orientation (this last step will make it easier to integrate the VDF to simulate an observation). This is done as follows:

$$f_{sc}(\vec{v}) = f_e \left(\vec{v} + \vec{V}_{sc} \right) \quad (3.5)$$

$$f_i(\vec{v}) = f_{sc} (\mathbf{R}' \cdot \vec{v}) \quad . \quad (3.6)$$

\vec{V}_{sc} is the spacecraft velocity in the ecliptic frame; f_{sc} is the velocity distribution in the spacecraft frame; f_i in the instrument frame (SPAN-A or SPC). \mathbf{R}' is the combination of a rotation from the detector orientation \vec{n} to \hat{z} followed by the rotation from \vec{m} to \hat{x} . The instrument orientation vectors are as defined in section 2.1.3 for SPAN-A and 2.2.2 for SPC.

Lastly, when observing particles, one wants to think in terms of *look direction*. When looking in a direction in space, an instrument is sampling particles coming *from* that direction which are therefore travelling in the *opposite* direction. And so

$$f_o(\vec{v}) = f_i(-\vec{v}) \quad , \quad (3.7)$$

f_o being the velocity distribution, in ecliptic coordinates, as seen by a detector.

3.2 Modelling SPAN-A Measurements

The flux J of particles per unit area per unit time can be expressed as:

$$J dW d\Omega = v^3 f(\vec{v}) dv d\Omega \quad , \quad (3.8)$$

where $d\Omega$ is solid angle and W is kinetic energy $dW = m v dv$, and f is the velocity distribution function in a chosen frame. Assuming a constant flux over a short integration time Δt , this gives

$$dN = A \Delta t f_o(\vec{v}) v^3 dv d\Omega \quad , \quad (3.9)$$

which, noting that $d\Omega = \sin(\theta) d\theta d\phi$, and integrating over a 'pixel' is [9]

$$N_{ijk} = A_{ij} \Delta t_{ij} \int_{v_k} \int_{\phi_i} \int_{\theta_j} f_o(\vec{v}) v^3 \sin(\theta) d\theta d\phi dv \quad . \quad (3.10)$$

Here, ϕ_i and θ_j are the range of solid angle covered by pixel (i, j) while v_k is the velocity band k . For an ESA, the width of this band is proportional to v and so a factor of v^4 is sometimes used (instead of v^3). However here the velocity bands will be entered into the program manually.

While Δt_{ij} and A_{ij} can technically vary depending on look direction (hence their subscript), here they are taken as constants. While no attempt is made to estimate these precisely, they are set to 1ms and 0.01m² respectively, reflecting the observation time-scale (see 2.1.2) and instrument size order of magnitudes.

3.3 Modelling SPC Measurements

Consider a Faraday cup and f_o such that the cup points in the \hat{z} direction. The cup has an effective area $A(\vec{v})$. By analogy to equation 3.9 for counts in a top-hat ESA, the current received by the Faraday cup (total over all plates) from an infinitesimal volume in velocity space, d^3v , is [15]

$$dI = e v A(\vec{v}) f_o(\vec{v}) d^3v \quad (3.11)$$

(e is the elementary charge) and so the current I_k in a z -velocity band $v_{z,k}$ is

$$I_k = e \int_{v_{z,k}} \int_{-\infty}^{+\infty} \int_{-\infty}^{+\infty} v A(\vec{v}) f_o(\vec{v}) dv_x dv_y dv_z . \quad (3.12)$$

Note that Cartesian coordinates are used for the integration. This is more natural for SPC since it distinguishes between z -velocities only.

Now, let us consider the fractional signal ratios V and W obtained by SPC. These were defined in section 2.2.3 and calculated for a uniform beam of particles. However the solar wind is not a uniform beam; to simulate SPC, one needs to integrate V and W over the VDF. In a given energy band k :

$$V_k = \left(e \iiint_k V(\vec{v}) v A(\vec{v}) f_o(\vec{v}) d^3v \right) / I_k \quad (3.13)$$

$$W_k = \left(e \iiint_k W(\vec{v}) v A(\vec{v}) f_o(\vec{v}) d^3v \right) / I_k \quad (3.14)$$

The triple integral is evaluated over the energy band k , corresponding to a planar slice in velocity space perpendicular to v_z . Note that, unlike in the integration for SPAN-A, it is not obvious which coordinates to use: while the integration volume is more natural in Cartesian coordinates, the signal ratios as well as the effective area are more easily expressed in terms of spherical polars. This is also true for the v factor in the integral. Cartesian are chosen here as they are ultimately easier to work with, especially regarding the integration limits.

One can easily notice that equations 2.9, 2.10 can be rewritten as

$$p = \arcsin[v_y/v] \quad \text{and} \quad t = -\arcsin[v_x/v] , \quad (3.15)$$

where $v = \sqrt{v_x^2 + v_y^2 + v_z^2}$ is implied. Similarly one can use $\theta = \arctan(v_z/v)$ to rewrite equation 2.12 (or any other cylindrically symmetric model) for the effective area $A(\theta)$. Explicitly, this gives

$$V_k = \left(e \int_{v_{z,k}} \int_{-\infty}^{+\infty} \int_{-\infty}^{+\infty} V\left(\frac{v_x}{v}\right) v A\left(\arctan\left(\frac{v_z}{v}\right)\right) f_o(v_x, v_y, v_z) dv_x dv_y dv_z \right) / I_k \quad (3.16)$$

$$W_k = \left(e \int_{v_{z,k}} \int_{-\infty}^{+\infty} \int_{-\infty}^{+\infty} W\left(\frac{v_y}{v}\right) v A\left(\arctan\left(\frac{v_z}{v}\right)\right) f_o(v_x, v_y, v_z) dv_x dv_y dv_z \right) / I_k \quad (3.17)$$

which can be easily integrated numerically.

3.4 Realistic Solar Wind Conditions

The power scaling law and values from Perrone et al. (2018) [17] for the density n , magnetic field strength $|B|$ and temperatures T_{\parallel} and T_{\perp} are used to obtain realistic conditions. The power law is:

$$f(R) = f_0 \left(\frac{R}{1\text{AU}} \right)^{\alpha} \quad (3.18)$$

The results of using this law are given in table 1; except for the solar wind velocity which is fixed at 700km s^{-1} , and the Alfvén speed at 200km s^{-1} .

Alfvén fluctuations are also included in the simulations, but only to assess whether they can shift the solar wind significantly into the field of view. As such, one wants to use the best possible scenario for a disturbance to occur. This best scenario would be one where the angle at which the solar wind hits the spacecraft is maximised, shifting the VDF more into the field of view of SPAN-A.

According to equation 1.4, for a fixed value of the ratio $R_B \equiv |\delta\vec{B}|/|B_0|$, the shift in velocity $\delta\vec{v}$ is $V_A R_B$ in the direction of $\delta\vec{B}$. However, while this direction depends on the initial magnetic field direction (since equation 3.3 has to be respected), the magnetic field direction in the wind is variable. Thus, when looking for a *best possible* scenario, the $\delta\vec{B}$ can be picked.

Two cases are explored: a normal fluctuation with $R_B = 1$ and a strong ‘switchback’ with $R_B = 2$, where the magnetic field direction is reversed. The $R_B = 1$ case corresponds to a 60° rotation of the field. In both cases, the velocity shift direction is chosen to maximise the incoming angle of the SW in the spacecraft frame.

4 Results & Analysis

4.1 Mission Statistics

Before looking at simulation results, it is worth thinking of the Parker Solar Probe mission as a whole. To do this planned trajectory data is used; the data gives the position of the spacecraft for each of the 2344 days of the mission. Mean daily velocities are obtained and projected into cylindrical components: radial, azimuthal and vertical (with respect to the ecliptic). These velocities are then added to a 700km s^{-1} solar wind velocity and the total angle of apparent solar wind from the radial direction is plotted as a histogram, figure 12. Only days with a spacecraft position closer than 54 Solar radii are included - these are the days of primary science operations [1] where the measurements matter most. The histogram is colour-coded: green bins are days where the centre of the velocity distribution is in the second SPAN-A anode pixel (one pixel is 11.25° wide); yellow bins show days where the centre is in the second half of the first pixel; red bins are days where the VDF centre is in the first half of the first pixel column, which is completely outside the field of view. Figure 5 shows the exact limit of the field of view (black line); notice the cropped pixel column on the very left. This should be kept in mind when looking at the simulation measurements below; while these show the first column, most of it will not actually be measured. One last thing to note here is that all the angles are below 30° , meaning that the solar wind stream is expected to stay well within SPC’s field of view at all times.

While in this work high speed solar wind streams at 700km s^{-1} are usually considered, the effect of different solar wind velocities is shown in figure 13. It shows the number of days that would have the VDF centre further than 0.5, 1, and 1.5 pixels away from the detector edge for different wind radial speeds. This is for a purely radial wind without disturbances.

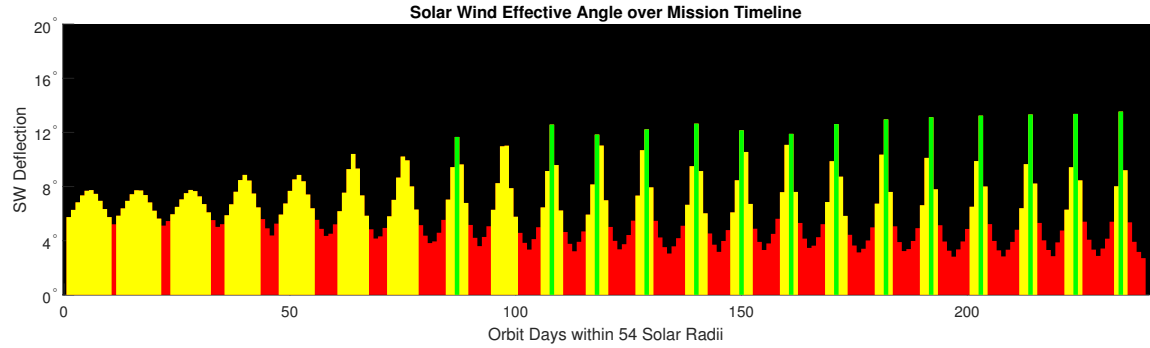


Figure 12: Effective angle of a radial, 700km s^{-1} solar wind over the duration of the PSP mission. Red bins show days with an angle less than 5.5° , yellow less than 11.25° and green above 11.25° .

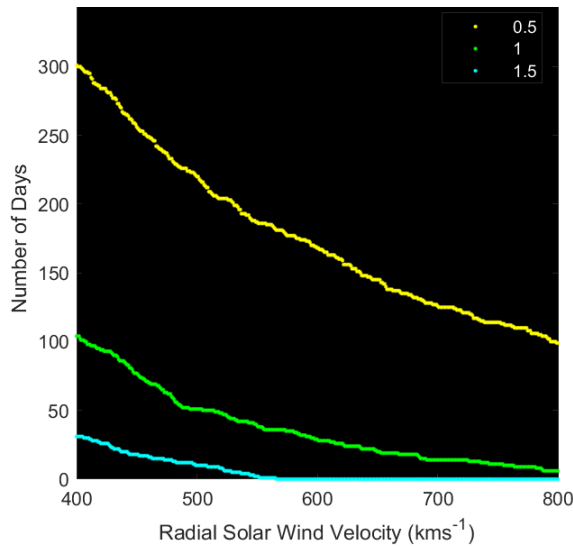


Figure 13: Total number of days during the mission where the VDF centre is within half, one or one and a half anode bands of the detector edge, depending on solar wind speed.

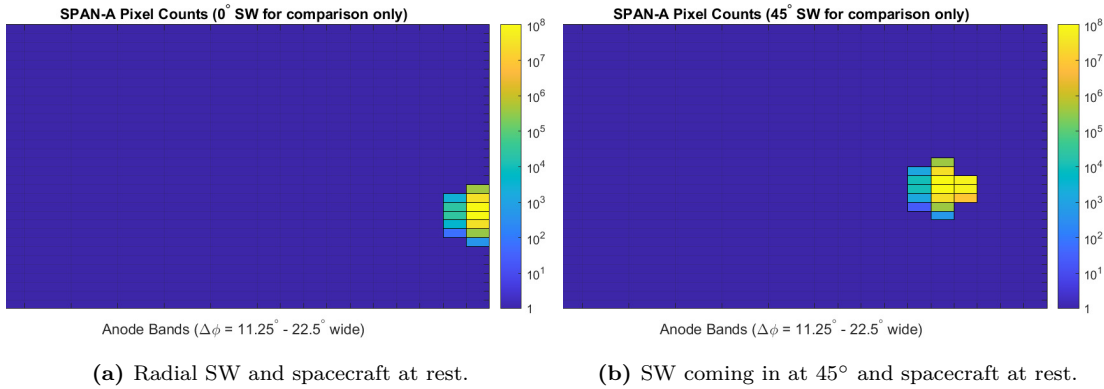


Figure 14: SPAN-A simulations for (imagined) solar wind incoming angles. Note that the very first column on the right would be partially obscured by the heat shield, as can be seen in figure 5 (on the left there). These are for a Solar Wind at $T_{||} = T_{\perp} = 10^5 K$.

4.2 Scenario Analysis

Before looking at specific scenarios, let us see what the response of SPAN-A looks like for very simple conditions. Figure 14 shows measurements for a purely radial wind and a wind coming in at a 45° angle from the ram direction, with no additional spacecraft velocity. In both cases the SW is at 700 km s^{-1} and 10^5 K in all directions. Note that this is quite cold compared to the temperatures used in 4.2 below, hence the very narrow signals. Note also, when looking at any of the simulation results, that SPAN-A is looking ‘upside down’ with respect to usual ecliptic coordinates. Thus the sunward direction is on the very right of the figures, while it is on the very left of figure 5 which shows the SPAN-A field of view, but *in ecliptic coordinates*.

What can be seen is that for a spacecraft at rest, almost none of the distribution would be seen past the first pixel column; meanwhile, shifting the SW to a 45° angle places the VDF almost perfectly within the field of view. In reality, intermediate angles to these should be expected.

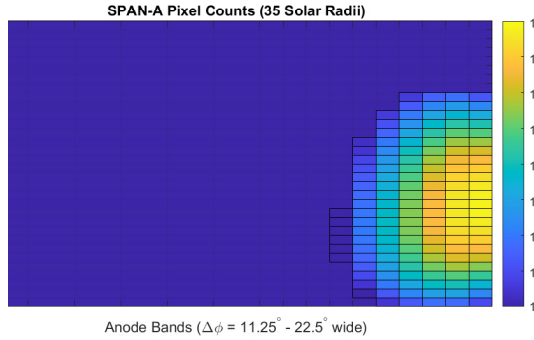
Two points in the probe’s orbit have been chosen to produce simulations of. The first is the first perihelion approach at ~ 35 solar radii (R_{\odot}); the second is the closest approach at $\sim 13 R_{\odot}$. The positions of the spacecraft and its velocities used are averages over one day. All the simulations have assumed a 700 km s^{-1} fast solar wind stream. The other plasma characteristics for these two points are obtained via equation 3.18 and summarised in table 1. Results for $35 R_{\odot}$ are shown in figure 15, results for $13 R_{\odot}$ in figure 16. The colour scale of the figures is logarithmic. All the SPAN-A simulations have been done over a large energy range of 5eV-10keV. Of course in reality the instrument will observe many smaller bands; however since the main concern is the location of the VDF within the field of view, this is appropriate.

While remembering that the first column of pixels is mostly outside the field of view (figure 5), it seems like some of the VDF will be recorded by SPAN-A during both these perihelion approaches (suggesting this might be true for all intermediate perihelia). Due to the complicated edge of the field of view, it would make little sense to compute an exact fraction of the VDF visible unless one were to include the exact shape of this edge into their computation.

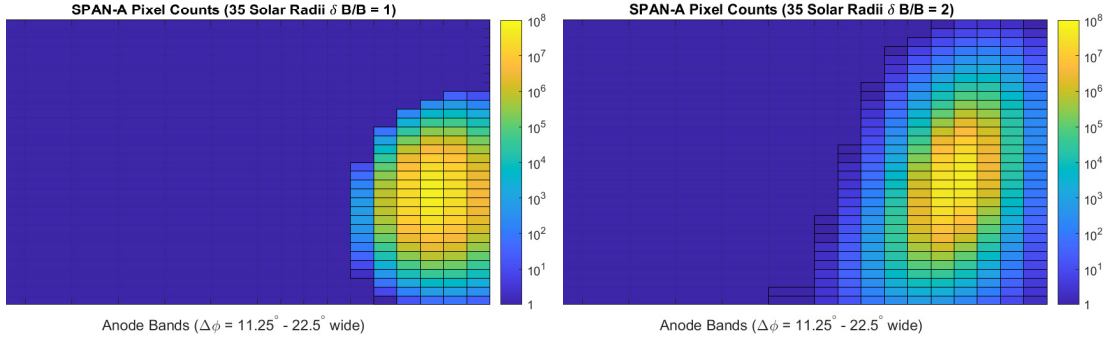
At 35 solar radii, what looks like about half of the distribution is seen due to large spacecraft speed (figure 15a), but a difference is clearly visible when fluctuations are fortunate: figure 15b contains almost all of the distribution while figure 15c shows the VDF nicely placed in the field of view.

Quantity & Units	First Approach	Last Approach
Distance from Sun R_{\odot}	35.8	13.1
Mission Day	93	2333
Radial Velocity (km s^{-1})	0.8	4.6
Azimuthal Velocity (km s^{-1})	95	157
Vertical Velocity (km s^{-1})	3.3	7.3
Magnetic Field Strength (nT)	104	538
T_{\perp} (10^5K)	13.1	34.8
T_{\parallel} (10^5K)	3.3	5.5
Number Density n (10^7 m^{-3})	9.6	78.0
V_A (km s^{-1})	200	200
Radial Solar Wind (km s^{-1})	700	700

Table 1: Solar Wind properties used in simulations, found by using the scaling law in Perrone et al. (2018) [17] - with the exceptions of radial wind and Alfvén speeds which are fixed.



(a) Radial SW with no Alfvénic fluctuations, at the first perihelion.



(b) Best possible scenario for a fluctuation with $\delta B/B = 1$. (c) Best possible scenario for a fluctuation with $\delta B/B = 2$.

Figure 15: SPAN-A simulations at $35R_{\odot}$. For values used, see table 1. The top figure is what is seen normally from the moving spacecraft. The lower figures show the best possible scenarios for Alfvén fluctuations (as described in section 1.3) with two fixed magnitudes.

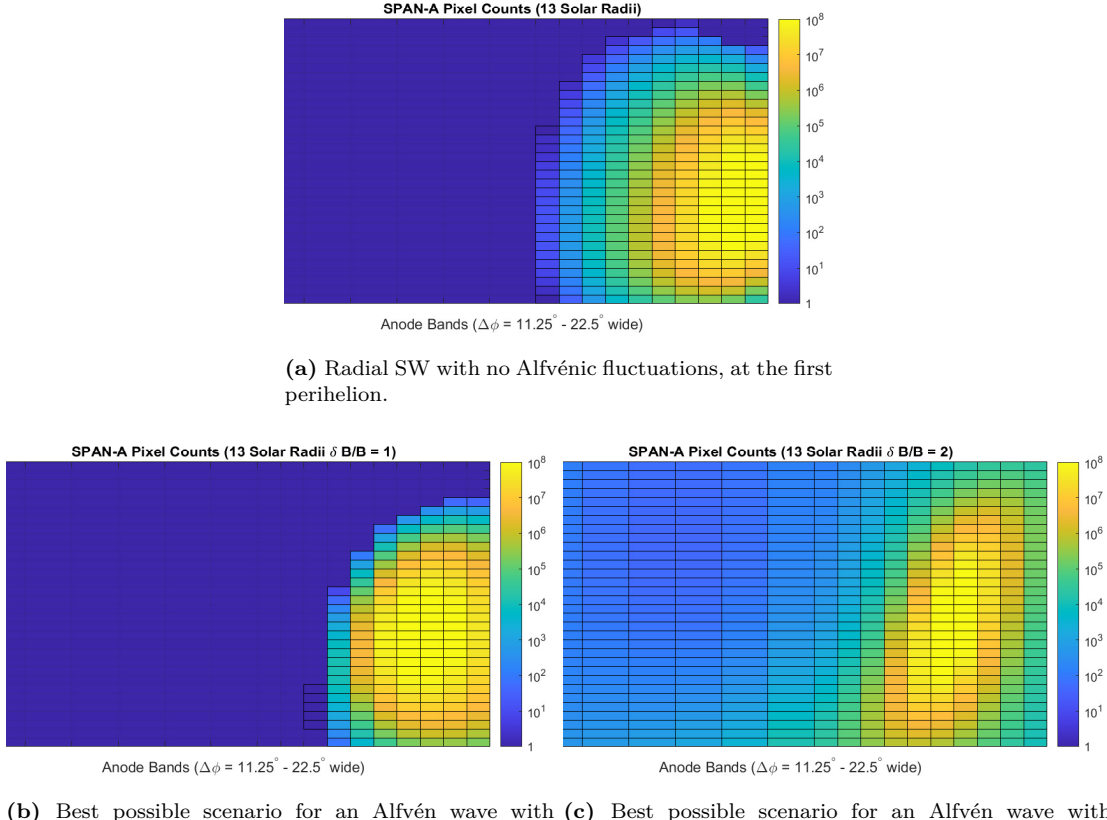


Figure 16: SPAN-A simulations at $13R_\odot$ (closest approach perihelion). As in figure 15, the top figure is what is seen normally from the moving spacecraft. The lower figures show the best possible scenarios for Alfvén fluctuations (as described in section 1.3) with two fixed magnitudes. For values used, see table 1.

	$35R_\odot$	$13R_\odot$
no fluctuations	1-2	2
$\delta b/ B = 1$	3	3
$\delta b/ B = 2$	4-5	4-5

Table 2: Summary of VDF centre locations, in number of pixel columns from right edge (as visually estimated looking at figures 16 and 15). Since at least the first half of the right pixel column is obstructed, this table shows that at first perihelion, only about half the distribution will be observed when no fluctuations are present. For the last perihelion, an additional half pixel column, or $\sim 5.5^\circ$ of the distribution should be visible (without fluctuations).

The VDF is quite wide: this is due to the rather large temperatures given by 3.18 : compare the size to the 10^5 K distributions shown in figure 14. However the position of the VDF in the field of view does not change with temperature, so these results are valid for a range of temperatures. The simulations show different VDF shapes; the magnetic field is in different directions as it is changed by the alfvénic fluctuations. Simulations at 13 solar radii (figure 16) show the same behaviour. A summary of VDF locations can be found in table 2. Notable is figure 16c: the VDF is shifted so much that some protons hit the detector from the anti-sunward direction (the left of the image is not empty).

4.3 Discussion

This section presents some of the limitations of this work, and possible extensions.

The main focus has been on the instruments; the solar wind model put through the simulations is very basic. Firstly, the VDF has been modelled as a simple bi-Maxwellian. However some solar wind protons are also found in higher velocity beam (as per section 1.3). Additionally, the solar wind proton velocity distribution core, while close to a bi-Maxwellian in its centre, is in fact better fitted by a Kappa distribution near its edges (see, e.g. Gerschmann et al. (2012) [18]). Ions other than protons have been neglected here, but in fact α particles and other ions are also of interest in the solar wind. For example, Maruca et al. (2013) [6] look at α particles to study the effect of collisions in the SW plasma. Thus it would be valuable to include them in instrument models. In addition, Faraday cups cannot distinguish between different particle masses: all ions are included in observations. A realistic simulation should therefore include them too.

Another area which could be extended on is the treatment of Alfvén fluctuations. The assumption that the magnetic field can be in any direction is sufficient to get an idea of the scale of influence of these fluctuations on the incoming SW direction; but if one wanted to get a statistical estimate of this direction the magnetic field would have to be considered. As mentioned before, the field forms a spiral; the angle between this spiral and the radial direction depends on the solar wind radial speed [9, 10].

This work uses fixed Alfvén and solar wind speed, with the latter corresponding to the fast solar wind only. A more comprehensive idea of field of view limitations would be obtained by including a wider range of wind conditions. This include a wider range of plasma conditions on PSP's path. More accuracy could also be achieved by using instantaneous velocities and position for PSP, instead of daily averages.

In terms of the instruments, extensions on this work should be more careful obtaining total counts and currents: it would be worthwhile finding the exact effective area for SPAN-A and any directional dependence, for example. It would also be reasonable to look at different instrument modes: scans that do not cover all of the pixels, and how the modes change the measurement time-scale.

Count statistics can also be simulated, as e.g. described in Paschmann & Daly [9]. While it seems here that count numbers are quite large (up to 10^8 counts in these SPAN-A simulations), considering real effective areas and times might change this. In addition, if the dynamic range of the anode detectors is not sufficient at high count rate, attenuators might be used, decreasing the count rates. One should also consider sources of false counts and how these can affect measurements [9].

To obtain the fraction of the VDF obtained at any point in the PSP trajectory, one would need to use the exact shape of the field of view obstructions shown in K15 (reproduced here in figure 5). This would be a rather useful step to perform, but would require somehow extracting the shape from that figure or obtaining it in some other way.

Finally, a natural follow up on this work would be to think *backwards*. Here, solar wind observations are approached as a forward problem: given a proton velocity distribution, what do the instruments record? However, to quantify the observation limitations associated with the heat shield, one would have to attempt *recovering* the VDF from simulated observations. This could be in terms of moments of the distribution, for example. Such an analysis of data with limited field of view is done by Gerschman et al. (2012) [18] for the MESSENGER mission.

Similarly SPC simulations results could be used to see if useful constraints on VDF shapes perpendicularly to the cup view direction can be determined. Moments analysis can be performed on any Faraday cup data [15] even with no partial signals, but this only considers the reduced distribution. According to K15 [1], SPC has an angular resolution of 1° , however this appears to be for a uniform stream only. In this context, as highlighted by K15, using four plates is redundant. However, for a distribution of velocity directions including an anisotropic core and maybe even a beam, using only three measurements (V , W and total counts) might be wasting valuable information. One could simulate measurements from, and find a method to use, four partial currents instead of two.

Conclusion

The framework presented here can be used for further simulations, with the aim of understanding field of view limitations or otherwise. In particular, the orientation vectors for SPAN-A and the description of the Solar Probe Cup geometry could be valuable as they are not found in the literature.

The discussion above shows that the simulations performed in this work are relatively simplistic. However they have given a good idea of what effect the spacecraft velocity and solar wind fluctuations can have on observations. The result of the simulations provide positive expectations for what can be measured with the SPAN-A instrument during the Parker Solar Probe mission. At least half of the proton velocity distribution should be sampled during perihelia for a fast radial wind; more should be seen for slower winds and in the case of fluctuations.

References

- [1] J. C. Kasper, R. Abiad, G. Austin, et al. Solar wind electrons alphas and protons (SWEAP) investigation: Design of the solar wind and coronal plasma instrument suite for solar probe plus. *Space Science Reviews*, 204(1-4):131–186, oct 2015.
- [2] N. J. Fox, M. C. Velli, S. D. Bale, et al. The solar probe plus mission: Humanity’s first visit to our star. *Space Science Reviews*, 204(1-4):7–48, nov 2015.
- [3] The Johns Hopkins University Applied Physics Laboratory. Where is Parker Solar Probe? [online], September 2018. <http://parkersolarprobe.jhuapl.edu/The-Mission/index.php#Where-Is-PSP>.

- [4] John C. Brandt. *Introduction to the Solar Wind*. W. H. Freeman and Company, 1970.
- [5] May-Britt Kallenrode. *Space Physics: An Introduction to Plasmas and Particles in the Heliosphere and Magnetospheres*. Springer, 1998.
- [6] B. A. Maruca, S. D. Bale, L. Sorriso-Valvo, J. C. Kasper, and M. L. Stevens. Collisional thermalization of hydrogen and helium in solar-wind plasma. *Physical Review Letters*, 111(24), dec 2013.
- [7] Lorenzo Matteini, Timothy S. Horbury, Marcia Neugebauer, and Bruce E. Goldstein. Dependence of solar wind speed on the local magnetic field orientation: Role of alfvénic fluctuations. *Geophysical Research Letters*, 41(2):259–265, jan 2014.
- [8] D. J. McComas, H. A. Elliott, N. A. Schwadron, et al. The three-dimensional solar wind around solar maximum. *Geophysical Research Letters*, 30(10):n/a–n/a, may 2003.
- [9] G. Paschmann and P. W. Daly, editors. *Analysis Methods for Multi-Spacecraft Data*. The International Space Science Institute, 1998.
- [10] Petr Hellinger, Pavel M. Trávníček, Štěpán Štverák, Lorenzo Matteini, and Marco Velli. Proton thermal energetics in the solar wind: Helios reloaded. *Journal of Geophysical Research: Space Physics*, 118(4):1351–1365, apr 2013.
- [11] J. W. Belcher and Leverett Davis. Large-amplitude alfvén waves in the interplanetary medium, 2. *Journal of Geophysical Research*, 76(16):3534–3563, jun 1971.
- [12] Roberto Bruno and Vincenzo Carbone. The solar wind as a turbulence laboratory. *Living Rev. Solar Phys.*, 2(4), 2005. [Online Article].
- [13] C.W. Carlson, D.W. Curtis, G. Paschmann, and W. Michel. An instrument for rapidly measuring plasma distribution functions with high resolution. *Advances in Space Research*, 2(7):67–70, jan 1982.
- [14] J. C. Kasper, A. J. Lazarus, J. T. Steinberg, K. W. Ogilvie, and A. Szabo. Physics-based tests to identify the accuracy of solar wind ion measurements: A case study with the wind faraday cups. *Journal of Geophysical Research*, 111(A3), 2006.
- [15] Bennett A. Maruca. Measurements of solar-wind ions with the wind/SWE faraday cups. Arcetri Turboplasmas School, Florence, Italy, October 2014.
- [16] M. Stevens and T. S. Horbury. Faraday cup geometry. Personal Communication, August 2018.
- [17] Denise Perrone, D. Stansby, T. Horbury, and L. Matteini. Radial evolution of the proton core temperature in pure high-speed streams: HELIOS revised observations. Manuscript in Preparation, August 2018.
- [18] Daniel J. Gershman, Thomas H. Zurbuchen, Lennard A. Fisk, et al. Solar wind alpha particles and heavy ions in the inner heliosphere observed with MESSENGER. *Journal of Geophysical Research: Space Physics*, 117(A12):n/a–n/a, sep 2012.
- [19] Serge Belongie. Rodrigues' rotation formula. *MathWorld*. A Wolfram Web Resource, created by Eric W. Weisstein. <http://mathworld.wolfram.com/RodriguesRotationFormula.html>.

Note: When a reference is placed after a full period, it refers to the whole preceding paragraph. References placed inside a sentence usually refer to that sentence only. Figures which are not referenced explicitly are my own.

A Appendix

A.1 Maths & Derivations

A.1.1 Notation

In this report, vectors (both in space and velocity space) are denoted with an arrow, such as \vec{u} . Unit vectors are denoted with a hat, e.g. \hat{x} ; matrices in bold, e.g. \mathbf{R} .

A.1.2 Area of a Disc Section

Take a disc of radius R , intersected by a line passing at distance B from its centre. The angle x is defined as in figure 17. Refer to this figure for the remainder of this section. Define $H(x)$ to be the relative area to the right of the line, A_1 , to the area to the left of the line, A_2 . That is

$$H(x) \equiv \frac{A_1 - A_2}{A_1 + A_2} \quad (\text{A.1})$$

Now, the area of the 'pie sector' $cdea$ is

$$A_3 = \pi R^2 \frac{2x}{2\pi} = xR^2 \quad , \quad (\text{A.2})$$

and the area of the triangle cda is

$$A_4 = B^2 \tan(x) = R^2 \sin(x)^2 \tan(x) = R^2 \sin(x) \cos(x) \quad . \quad (\text{A.3})$$

Noting that $A_2 = A_3 - A_4$, and that $A_1 = \pi R^2 - A_2$, one can write

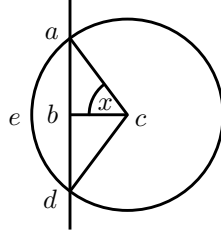


Figure 17: Cut disc, featuring angle x and points a, b, c, d and e .

$$H(x) = \frac{\pi R^2 - 2A_2}{\pi R^2} = 1 + \frac{2A_4}{\pi R^2} - \frac{2A_3}{\pi R^2} \quad ; \quad (\text{A.4})$$

i.e.

$$H(x) = 1 + \frac{2}{\pi} (\sin(x) \cos(x) - x) \quad , \quad (\text{A.5})$$

as in equation 2.4 used in section 2.2.3.

A.1.3 Rodrigues' Rotation Formula

Rodrigues' rotation formula gives the matrix corresponding to a rotation by an angle α about an axis defined by unit vector $\vec{\omega}$. The rotation matrix is given by: [19]

$$\mathbf{R} = \mathbb{I} + \tilde{\omega} \sin(\alpha) + \tilde{\omega}^2 (1 - \cos(\alpha)) \quad , \quad (\text{A.6})$$

where \mathbb{I} is the identity matrix, and $\tilde{\omega}$ is the matrix which, applied to a vector on the left is equivalent to taking the cross product of $\vec{\omega}$ on the left. This implies

$$\tilde{\omega} \equiv \begin{bmatrix} 0 & -\omega_z & \omega_y \\ \omega_z & 0 & -\omega_x \\ -\omega_y & \omega_x & 0 \end{bmatrix} , \quad (\text{A.7})$$

where $\omega_x, \omega_y, \omega_z$ are the components of $\vec{\omega}$. Additionally, one should note that

$$\tilde{\omega}^2 = \vec{\omega} \otimes \vec{\omega} - \mathbb{I} , \quad (\text{A.8})$$

which can be shown directly from A.7 and remembering that $\omega_x^2 + \omega_y^2 + \omega_z^2 = 1$ since $\vec{\omega}$ is a unit vector. Substituting this into equation A.6 gives equation 3.4.

A.2 Acknowledgements

I would first like to thank my supervisor, Prof. Tim Horbury, not only for making this project possible but also enjoyable. Thank you for taking plenty of time to discuss this work with me.

I also thank Dr. Ben Maruca for discussion and providing me with his lecture notes on Faraday cups; David Stansby for sending me his code and trajectory data for PSP; Dr. Michael Stevens for sending information on the Faraday cup effective area and relative signals.

I thank my fellow MSc Physics classmates for discussions, friendship and many snack breaks. Thank you also to my non-physicist friends who have given moral support and shown interest in my work. I owe most to my family, who always encourage me in my studies.

Lastly, I would like to thank the Parker Solar Probe team around the world; I am thankful that this mission has been made possible and that I can have some involvement in it.

A.3 Declaration of Work

I have written all the code used in this work, with the exception of the spacecraft trajectory code, which I have used data from. All the diagrams and figures are mine unless referenced explicitly. I have written this report myself.

While none of the physics in this report is new; I have compiled all the relevant equations myself and derived some of them; I have re-derived all of the geometry. Single equations are sometimes taken out of books and papers, but never a whole derivation or sequence of equations.